Thermochronology constraints for the propagation sequence of the south Pyrenean basement thrust system (France-Spain)

Marc Jolivet, Pierre Labaume, Patrick Monie, Maurice Brunel, Nicolas Arnaud, M. Campani

Thermochronology constraints for the propagation sequence of the south Pyrenean basement thrust system (France-Spain)

Marc Jolivet,[1] Pierre Labaume,[1] Patrick Monié,[1] Maurice Brunel,[1] Nicolas Arnaud,[1] and Marion Campani[1,2]

Received 13 November 2006; revised 21 May 2007; accepted 6 June 2007; published 28 September 2007.

[1] In this work we combined apatite fission track and biotite/K-feldspar $^{40}Ar/^{39}Ar$ ages with tectonic data in the west central part of the Axial Zone of the Pyrenees. We discuss the exhumation ages and rates of the Néouvielle, Bordère-Louron, and Bielsa Variscan granites and their relationships with the timing and sequence of south vergent basement thrusting within the Pyrenean orogenic prism. The $^{40}Ar/^{39}Ar$ ages on K-feldspars from the Néouvielle massif (sample NV7) seem to indicate tectonic movements on the Eaux-Chaudes thrust during the early middle Eocene. Fission track results suggest that the exhumation of the Néouvielle massif occurred around 35 Ma and exhumation of the Bordère-Louron massif around 32 Ma in relation to thrusting on the Gavarnie thrust. The Bielsa massif was exhumed from around 19 Ma by out-of-sequence movements on the Bielsa thrust. We thus show that whereas most of the Pyrenean basement thrust faults (here the Eaux-Chaudes, Gavarnie, and Guarga thrusts) were active in sequence toward the southern foreland from the early Eocene to the earliest Miocene, some of them (here the Bielsa thrust) were activated out of sequence in the hinterland, later than the generally accepted Aquitanian age for the end of the Pyrenean compression. Finally, the apatite fission track modeling indicate a last cooling episode starting around 5 Ma which is most certainly related to the Pliocene reexcavation of the southern and northern flanks of the Pyrenees. **Citation:** Jolivet, M., P. Labaume, P. Monié, M. Brunel, N. Arnaud, and M. Campani (2007), Thermochronology constraints for the propagation sequence of the south Pyrenean basement thrust system (France-Spain), *Tectonics*, *26*, TC5007, doi:10.1029/2006TC002080.

1. Introduction

[2] Convergence and collision between tectonic plates lead to the formation of an accretionary prism that generally involves both the sedimentary cover and the basement. Complex interaction between tectonic propagation of the prism, relief building, subsequent erosion and sediment transport toward a foreland basin then develop. The kinematics of those processes of deformation, erosion and sedimentation within an accretionary prism remain to be described in terms of timing, rate and magnitude.

[3] The Pyrenees belt is a Late Cretaceous-Tertiary intracontinental collision zone that developed between Iberia and Europe. The Axial Zone and the south Pyrenean foreland basin form a typical accretionary prism with a southward vergence. Its general tectonic structure and the tectonic-sedimentation relationships inside the foreland basin are well known [e.g., *Séguret*, 1972; *Labaume et al.*, 1985; *Muñoz*, 1992; *Teixell*, 1996; *Teixell and Muñoz*, 2000; *Millán Garrido et al.*, 2000; *Vergés et al.*, 2002], but only a few geochronological data are available to constrain the evolution of the prism, mostly in the central part of the Axial Zone [*Morris et al.*, 1998; *Fitzgerald et al.*, 1999; *Maurel*, 2003; *Sinclair et al.*, 2005].

[4] In this paper we coupled a tectonic study of the Néouvielle, Bordère-Louron and Bielsa Variscan granite massifs with apatite fission track and biotite/K-feldspar $^{40}Ar/^{39}Ar$ analyses to describe the tectonic exhumation of the west central Axial Zone. Burying and exhumation of those granite massifs were controlled by major basement thrusts, from north to south the Eaux-Chaudes, Gavarnie, and Bielsa thrusts in the Axial Zone and the Guarga thrust below the northern part of the foreland basin. One aim of this study is to precisely date the timing and sequence of thrusting in this part of the Axial Zone by looking at the exhumation age and rate of the granites. This in turn provides implications for tectonic deformation in the foreland basin.

2. Geological Setting

[5] The Pyrenees formed during the Late Cretaceous-Tertiary collision between the Iberian and European lithospheric plates [*Muñoz*, 1992]. The wedge comprises a major south vergent thrust system constituted by (1) an antiformal stack of basement units that expose Paleozoic rocks and form the Axial Zone of the belt, passing southward to (2) decolled and imbricated Meso-Cenozoic successions that form the South Pyrenean Zone (SPZ [*Séguret*, 1972; *Muñoz*, 1992]) (Figures 1 and 2). The oldest (Late Cretaceous to early Oligocene) depocenters of the foreland basin have been integrated in the SPZ (the Jaca, Ainsa, Tremp, and Ripoll piggyback basins in Figure 1). South of the SPZ, the Ebro basin corresponds to the most recent, late Eocene to early Miocene depocenter. Growth strata show that

[1]Laboratoire Géosciences Montpellier, CNRS-UMR 5243, Université Montpellier II, Montpellier, France.
[2]Now at Geology Institute, ETH Zentrum, Zurich, Switzerland.

0278-7407/07/2006TC002080

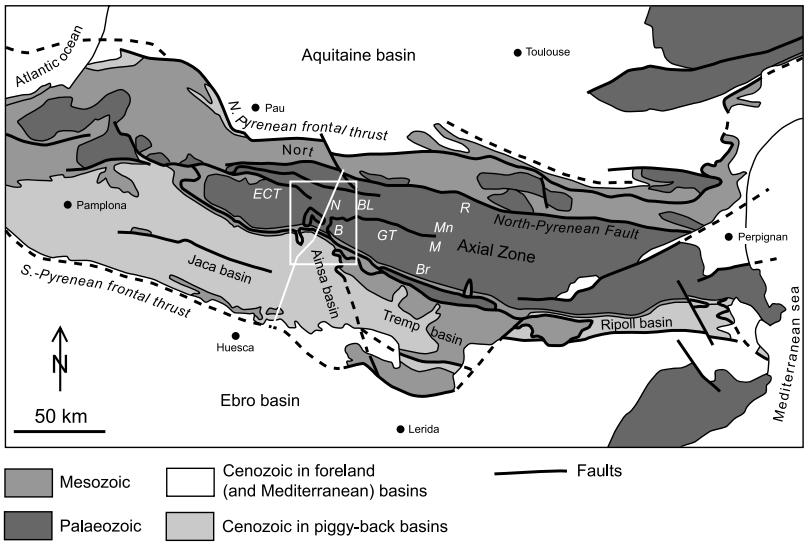

Figure 1. Structural map of the Pyrenees (simplified after *Teixell* [1996]). ECT, Eaux-Chaudes thrust; GT, Gavarnie thrust. Granite massifs are B, Bielsa; BL, Bordère-Louron; Br, Barruera; M, Maladetta; Mn, Marimanya; N, Néouvielle; R, Riberot. White frame indicates location of the studied area (compare Figure 3); white line indicates section in Figure 2.

compression along the south Pyrenean thrust front ceased during the early Miocene [*Teixell*, 1996; *Millán Garrido et al.*, 2000; *Teixell and Muñoz*, 2000; *Arenas et al.*, 2001]. To the north, the North Pyrenean Zone is a north vergent, back thrust system.

[6] Shortening has been estimated from 100 km [*Roure et al.*, 1989] to 165 km [*Beaumont et al.*, 2000] in the central part of the belt and to 80 km in the western part [*Teixell*, 1998]. The granite massifs studied here were emplaced across Paleozoic metasediments at the end of the Variscan orogeny [*Gleizes et al.*, 2001; *Román-Berdiel et al.*, 2004]. They are diversely located with respect to the three south vergent major basement thrusts of the western Axial Zone, which are from north to south the Eaux-Chaudes, Gavarnie, and Bielsa thrusts (Figures 1, 2, and 3). The Néouvielle massif is enveloped by several branches of the Eaux-Chaudes thrust that splays eastward, i.e., the Pic du Midi thrust to the north of the massif, a set of steeply dipping, mainly reverse, alpine shear zones that cut the massif with minor offsets [*Lamouroux et al.*, 1979; *Henderson and McCaig*, 1996; *Ingles et al.*, 1999], and the Pic-Long thrust along the southern border of the massif. The minor Piau-Engaly intrusion is a satellite of the Néouvielle massif located in the footwall of the Pic-Long thrust. The Néouvielle, Piau-Engaly, and Bordère-Louron massifs are located in the hanging wall of the major Gavarnie thrust, whereas the Bielsa massif is located just in the footwall. The Bielsa massif is itself in the hanging wall of the Bielsa thrust, which does not outcrop but caused the uplift and tilting of the southern edge of the Axial Zone, including the Bielsa granite and the overlying Gavarnie thrust sheet [*Casas et al.*, 2003]. Below the Jaca basin, the Guargua thrust is the southernmost basement thrust [*Teixell*, 1996]. The Monte Perdido thrust which affects the cover sediments in the northern part of the Jaca and Ainsa basins probably

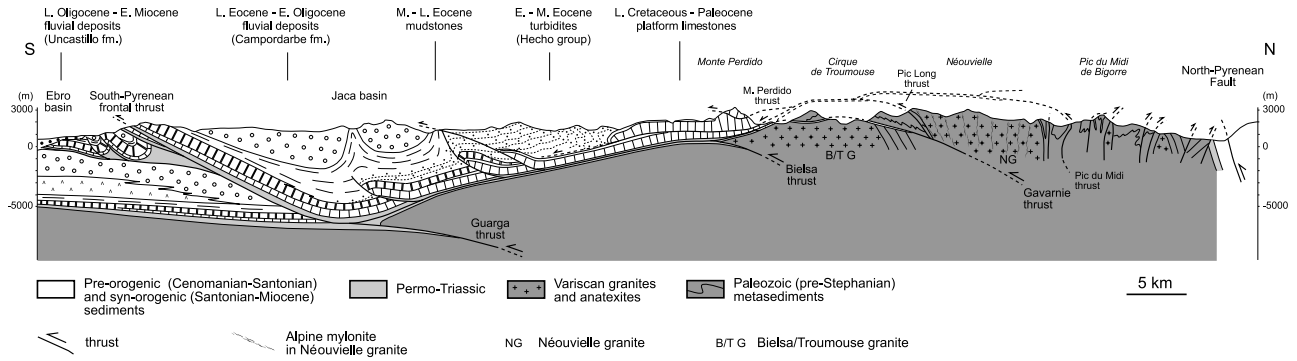

Figure 2. Structural cross section of the Axial Zone and Jaca basin (location in Figure 1). Structure of the south Pyrenean frontal thrust and southern Jaca basin modified from *Millán Garrido et al.* [2000]; northern Jaca basin modified from *Mutti et al.* [1988] and *Millán Garrido et al.* [2006].

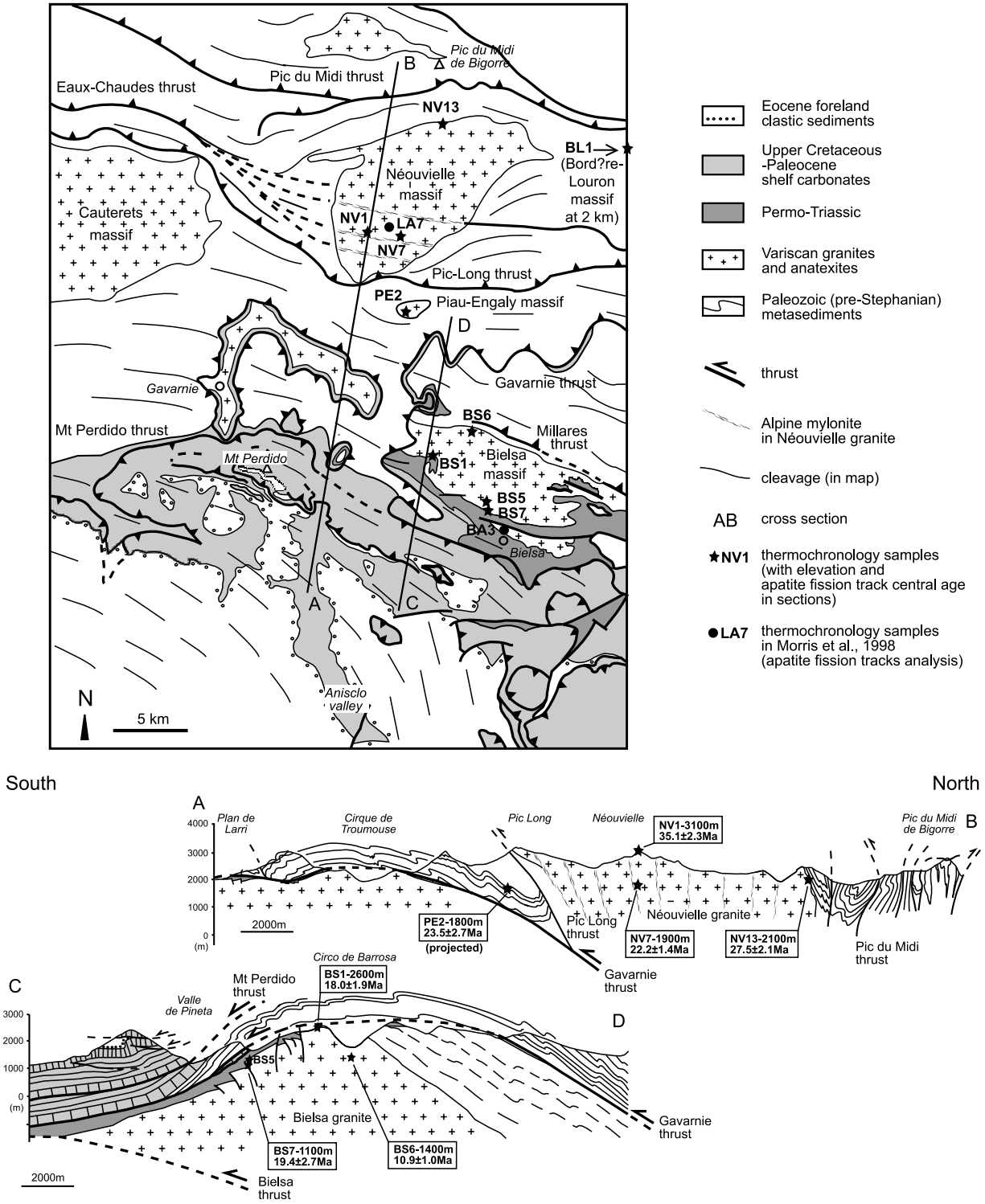

Figure 3. Structural map and cross sections of the studied area (location in Figure 1), with location of samples and indication of apatite fission track central ages.

Table 1. The $^{40}Ar/^{39}Ar$ Analytical Data for Biotites[a]

Step	40/39	38/39	37/39	36/39 (E-3)	F39Ar Released	%40*	40*/39K	Age, Ma	Error, Ma
					NV1 Biotite				
1	598.129	0.432	0.28512	1994.029	0.16	1.49	8.89	41.59	465.26
2	62.792	0.110	0.09354	193.840	0.47	8.76	5.50	88.85	25.78
3	17.969	0.057	0.00926	12.404	9.59	79.49	14.28	222.34	1.11
4	13.738	0.056	0.04702	5.314	14.51	88.44	12.15	190.83	1.19
5	13.664	0.048	0.01162	1.509	42.43	96.60	13.20	206.37	0.29
6	14.076	0.005	0.00229	0.653	56.61	98.49	13.86	216.16	0.73
7	14.096	0.005	0.01046	0.911	68.99	97.95	13.81	215.34	0.74
8	12.793	0.000	0.04974	0.549	73.12	98.60	12.61	197.71	1.81
9	13.264	0.002	0.01006	0.060	77.30	99.72	13.23	206.79	1.39
10	14.104	0.001	0.01096	0.345	86.18	99.14	13.98	217.92	0.62
11	13.912	0.001	0.05886	1.233	93.32	97.26	13.53	211.29	0.83
12	13.832	0.001	0.06357	3.767	95.97	91.84	12.70	199.04	1.86
13	13.490	0.001	0.05822	2.225	100.00	95.00	12.82	200.72	1.46
					NV7 Biotite				
1	1755.494	1.134	0.78316	5886.424	0.06	0.92	16.09	248.61	1219.06
2	117.922	0.192	0.30951	396.387	0.26	0.67	0.79	13.01	39.80
3	19.047	0.059	0.01203	14.846	4.83	76.87	14.64	227.56	3.33
4	15.904	0.063	0.03174	3.425	6.36	93.52	14.87	230.95	1.99
5	15.830	0.042	0.00755	2.217	16.80	95.74	15.16	235.06	1.51
6	15.758	0.068	0.00071	0.586	24.54	98.78	15.57	241.00	0.52
7	15.808	0.061	0.00260	0.998	30.85	98.01	15.49	239.96	1.06
8	15.645	0.059	0.00351	0.331	47.34	99.25	15.53	240.45	0.78
9	15.836	0.063	0.00102	0.767	53.88	98.44	15.59	241.35	0.78
10	15.902	0.072	0.00010	0.000	57.54	99.87	15.88	245.59	0.52
11	15.815	0.062	0.00285	0.410	67.30	99.11	15.67	242.58	0.75
12	15.688	0.063	0.00728	0.342	75.35	99.23	15.57	241.03	0.84
13	15.300	0.068	0.00655	0.949	81.02	98.04	15.00	232.79	1.20
14	15.116	0.060	0.01305	0.781	90.28	98.35	14.87	230.84	0.58
15	14.531	0.061	0.01733	0.000	93.83	99.86	14.51	225.67	1.29
16	14.834	0.062	0.08155	2.032	96.67	95.85	14.22	221.38	1.15
17	14.324	0.067	0.09204	1.564	100.00	96.67	13.85	215.94	1.03
					BS5 Biotite				
1	90.173	0.142	0.0000	260.558	0.36	14.59	13.16	205.76	20.79
2	14.902	0.072	0.1647	10.618	6.51	78.88	11.76	184.93	0.94
3	17.178	0.077	0.0815	0.000	10.74	99.88	17.16	264.02	1.19
4	16.865	0.069	0.2160	3.958	15.30	93.02	15.69	242.82	2.12
5	16.330	0.063	0.0935	0.688	44.37	98.67	16.11	248.92	0.77
6	17.306	0.064	0.0187	0.000	49.30	99.88	17.29	265.78	1.21
7	17.065	0.059	0.0339	0.282	57.49	99.41	16.96	261.16	1.03
8	16.391	0.063	0.0174	0.000	62.07	99.88	16.37	252.66	0.85
9	15.699	0.060	0.0176	0.162	75.53	99.57	15.63	241.97	0.79
10	17.014	0.062	0.0371	0.708	79.70	98.67	16.79	258.62	1.58
11	17.555	0.068	0.0203	0.000	83.64	99.89	17.54	269.34	1.35
12	18.234	0.067	0.0416	0.330	91.89	99.37	18.12	277.65	0.89
13	18.172	0.064	0.3933	0.433	95.14	99.32	18.05	276.69	1.29
14	18.540	0.061	0.5632	3.673	96.67	94.22	17.48	268.47	2.17
15	18.602	0.059	0.4323	0.993	100.00	98.46	18.32	280.50	1.36
					BS6 Biotite				
	18.834	0.096	0.00000	0.315	6.95	99.40	18.72	286.17	0.76
	18.751	0.107	0.00093	0.537	29.67	99.05	18.57	284.07	0.31
	18.834	0.099	0.00088	0.598	36.98	98.96	18.64	284.99	0.94
	18.940	0.102	0.00244	0.599	47.38	98.96	18.74	286.48	0.49
	18.676	0.094	0.00169	1.122	60.14	98.12	18.32	280.55	0.93
	18.360	0.097	0.00358	0.271	68.98	99.46	18.26	279.64	0.92
	17.623	0.091	0.00647	1.512	72.51	97.35	17.16	263.93	1.37
	17.666	0.098	0.00000	1.510	75.05	97.36	17.20	264.53	1.31
	17.853	0.118	0.00506	0.025	84.43	99.85	17.83	273.48	0.83
	18.143	0.111	0.00827	0.947	88.24	98.35	17.84	273.73	0.90
	18.428	0.103	0.02074	0.879	92.91	98.49	18.15	278.07	1.17
	18.803	0.112	0.02717	1.066	95.11	98.23	18.47	282.62	1.59
	18.385	0.115	0.05334	0.126	100.00	99.71	18.33	280.66	0.81

[a]J = 0.009182. Total ages are 209.8 ± 2.1 for NV1 biotite, 236.2 ± 2.5 for NV7 biotite, 249.5 ± 2.4 for BS5 biotite, and 277.3 ± 2.6 for BS6 biotite.

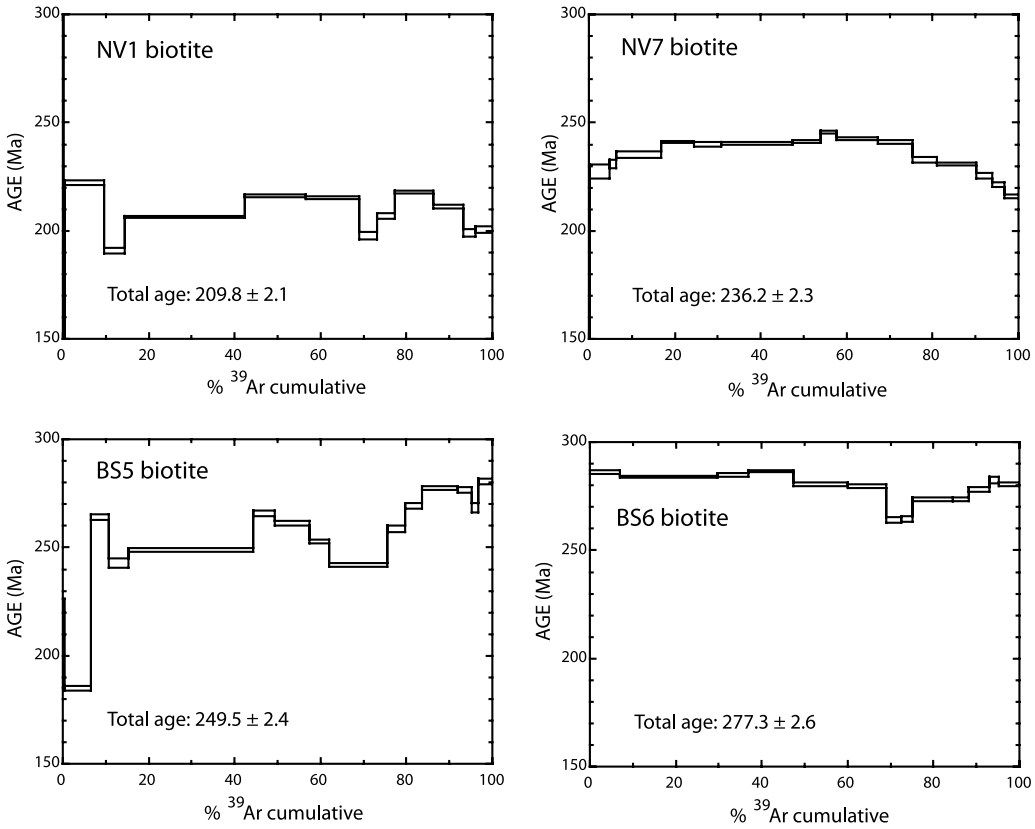

Figure 4. Biotite $^{40}Ar/^{39}Ar$ age spectra for the Néouvielle and Bielsa massifs.

roots in the Eaux-Chaudes thrust [*Labaume et al.*, 1985; *Teixell*, 1996].

3. Thermochronology

3.1. Sampling

[7] The location of the nine samples was chosen to recover the thermal history of the different granite massifs during their burial and subsequent exhumation during the Pyrenean orogeny, and derive constraints for the timing of activity of the major basement thrusts (see location of samples in Figure 3). In particular, emplacement of the Gavarnie thrust should have participated to the uplift of the Néouvielle, Piau-Engaly, and Bordère-Louron massifs in its hanging wall and to the burial of the Bielsa massif in its footwall. The latter massif and the overlying Gavarnie thrust sheet were then uplifted and tilted by the Bielsa thrust. Vertical sampling profiles should constrain exhumation rates, whereas age variations along horizontal or inclined profiles may reflect differential exhumation generated by thrust-related tilting or offset in each thrust compartment [e.g., *Fitzgerald et al.*, 2006]. In the Néouvielle (including Piau-Engaly) massif, the NV1 (summit) and NV7 (base) samples correspond to a subvertical profile with 1200 m of altitude difference, whereas samples NV13, NV7 and PE2 form a 13 km long, subhorizontal profile at an altitude of ~2000 m, subparallel to thrust motion and crossing the Néouvielle massif and the Pic-Long thrust. Furthermore, the NV1 and BL1 samples form an along-strike profile between the tops of the Néouvielle and Bordère-Louron massifs that display an elevation difference of 2200 m for a horizontal distance of 20 km. In the Bielsa massif, the summit sample (BS1) is at the top of two sampling profiles, one with sample BS6 (altitude difference of 1200 m) and one with samples BS5 and BS7 (altitude difference of 1400 m and 1500 m, respectively). Specificity of the BS1-BS5-BS7 profile is that the three samples are located just below the Permian-Cretaceous tilted unconformity, that corresponds to the horizontal prior to the Pyrenean tectonic phase and now dips about 35–40° southward. By contrast, the other valley sample (BS6) is located in the core of the massif. All samples are undeformed granitoids and sampling profiles were performed as much as possible in the same lithology.

3.2. Ar/Ar Methodology

[8] Five samples were selected for $^{40}Ar/^{39}Ar$ analyses, two in the Néouvielle massif (NV1 and NV7) and three others in the Bielsa massif (BS1, BS5 and BS6; Figure 3). Biotite single grains (in NV1, NV7, BS5 and BS6) and K-feldspar bulk separates (in NV1, NV7, BS1 and BS6) were analyzed using step-heating laser probe and furnace argon extraction methodologies, respectively. Analytical procedures for both extraction methods have been already pub-

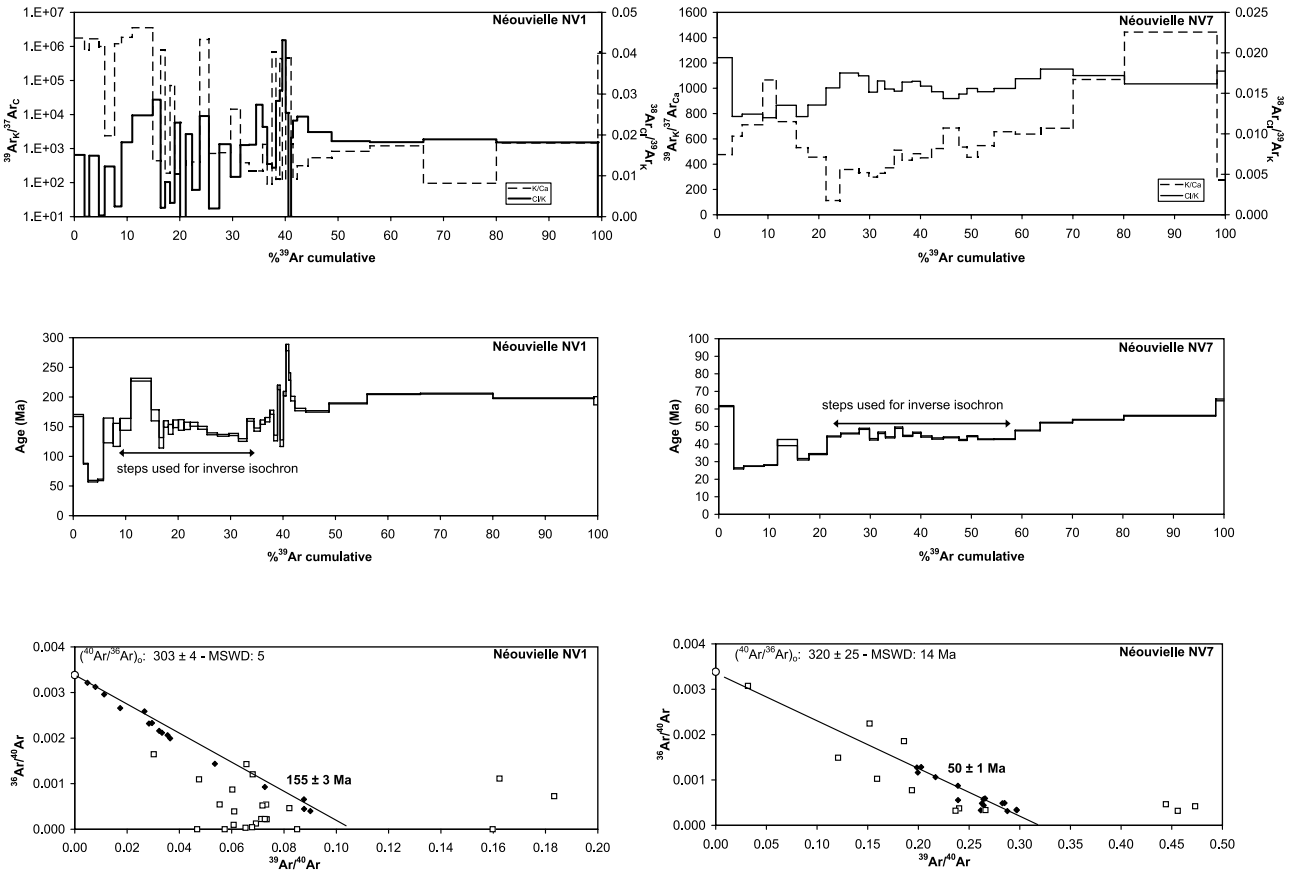

Figure 5. K-feldspar correlation plots for the Néouvielle and Bielsa massifs $^{40}Ar/^{39}Ar$ analysis. For each sample, spectra represent (top) $^{39}Ar/^{37}Ar$ and $^{38}Ar/^{39}Ar$ spectra used as proxies for K/Ca and Cl/K ratios, respectively; (middle) age spectra and (bottom) inverse isochron diagram with ages and statistical data when calculated. Black diamonds on inverse isochrons are points used for the calculations, while white squares are excluded data. Note the correlation between Cl/K and age spectra plots in the first 40% of ^{39}Ar release, suggesting excess argon released from fluid inclusions.

lished [*Monié et al.*, 1997; *Arnaud et al.*, 2003; *Maurel et al.*, 2004], and only a few details are given thereafter. After separation and irradiation at the McMaster nuclear reactor, biotite single grains were stepwise heated using a continuous, defocused argon laser beam and released and purified argon was analyzed on the electron multiplier of a MAP215-50 mass spectrometer. Each analysis involves 5 min for lasering and gas cleaning and 15 min for data acquisition by peak switching from mass 40 to 36, through 10 sets of data. System blanks were evaluated every three analyses and range around 2×10^{-12} cm^3 for ^{40}Ar and 3×10^{-14} cm^3 for ^{36}Ar. For K-feldspar analyses, the irradiated minerals were loaded into a double vacuum Staudacher type furnace which temperature is calibrated by means of a thermocouple placed at the base of the crucible. Each step includes 20 min of heating and 5 min of cleaning on Al-Zr getters and cold traps and 12 min of measurement on a VG3600 mass spectrometer. Signals were collected on a Faraday cup for ^{40}Ar and ^{39}Ar while ^{39}Ar, ^{38}Ar, ^{37}Ar and ^{36}Ar were analyzed with a photomultiplier after interaction on a Daly plate. For each individual age reported in Table 1, usual isotope corrections including blanks, mass discrimination radioactive decay of ^{37}Ar and ^{39}Ar and irradiation-induced mass interference were applied. Error reported for individual step takes into account the errors introduced by these corrections as well as the analytical errors on signals. Error on the J factor was propagated in the calculation of the total age of each sample, equivalent to a K-Ar age. A peculiar step heating schedule was conducted on K-feldspar in order to identify excess from possible fluid inclusions and retrieve diffusion characteristics [*Harrison et al.*, 1991; *Lovera et al.*, 1989, 1991]. We thus conducted duplicated isothermal step heating at low temperatures (450–800°C), often yielding a sawtooth-shaped age spectrum where the second of the two stages is systematically younger and probably less affected by excess argon [e.g., *Harrison et al.*, 1994].

3.3. Ar/Ar Results

[9] Ages obtained using $^{39}Ar/^{40}Ar$ analysis on biotite correspond to cooling through temperatures of ~300 ±

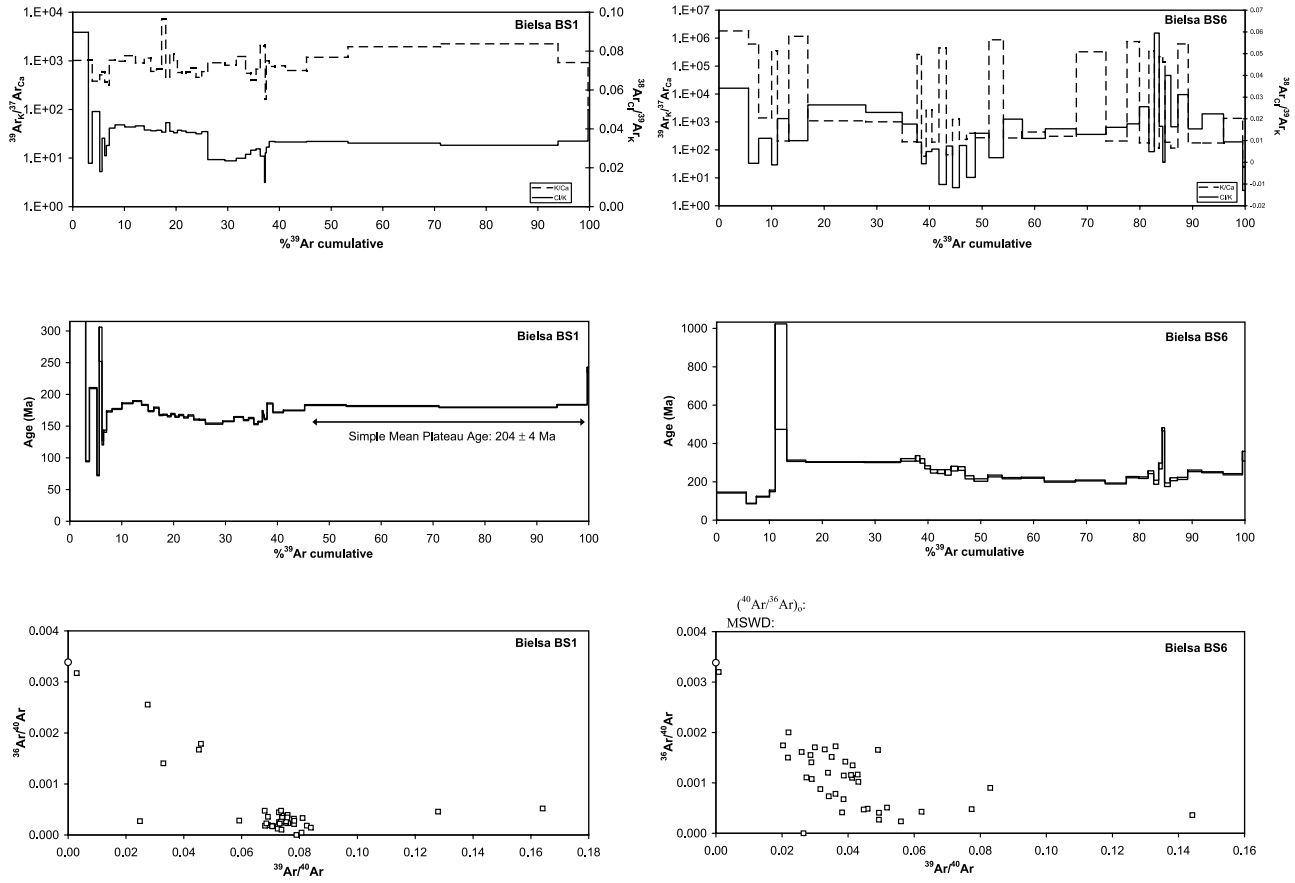

Figure 5. (continued)

50°C [*Dodson*, 1973; *Harrison and Armstrong*, 1978], while $^{39}Ar/^{40}Ar$ analysis on K-feldspar were made to allow continuous modeling of the temperature-time path between ~150 and 250°C [*Lovera et al.*, 1989; *Lovera*, 1992]. The four biotite age spectra are reported on Figure 4. The age spectra are variably discordant, with total ages ranging from 209.8 ± 2.1 Ma to 277.3 ± 2.6 Ma and individual ages scattering mainly from 185 Ma to 286 Ma, thus attesting for variable degree of partial resetting of these late Variscan biotites during the Pyrenean orogeny. No plateau or intercept age in the $^{36}Ar/^{40}Ar$versus$^{39}Ar/^{40}Ar$ correlation plot can be calculated with the present data. The total ages are younger in the Néouvielle massif (209.8 ± 2.1 Ma and 236.2 ± 2.3 Ma for samples NV1 and NV7, respectively) than in the Bielsa massif (249.5 ± 2.4 Ma and 277.3 ± 2.6 Ma for samples BS5 and BS6, respectively) and, for both massifs, older in their core than on the summit or below the Permian unconformity.

[10] All feldspars show very scattered age spectra (Figure 5). Notably, and for all samples, there is a strong correlation between ages and $^{38}Ar/^{39}Ar$ ratios (a proxy for Cl/K ratios; Table 2), probably underlying the presence of excess argon from decrepitating fluid inclusions. Excess argon thus strongly complicates the interpretation of the spectra. Most samples show a range of Mesozoic ages which we interpret to be intermediate values between the Variscan magmatic ages and later cooling, and thus total fusion ages are not meaningful. Even the use of the inverse isochron plot does not help resolve ages from Bielsa samples, although average ages of 180–200 Ma are suggested with large regression errors (MSWD>10), in agreement with larger steps obtained at higher degassing temperatures (on BS1 for example). For sample NV1 from the top of the Néouvielle granite, the inverse isochron allows to calculate an age of 155 ± 3 Ma for the first part of the age spectrum (the one dominated by excess argon) with a reasonable MSWD (5). Sample NV7 has a total age of circa 53 Ma but shows a range of ages starting from Oligocene ages at low temperature of degassing, to an intermediate pseudoplateau around 50 Ma, which is the part in which excess argon from fluid inclusions is the most prominent, and finally increasing to upper Cretaceous ages. The use of inverse isochron on the intermediate flatter part yields an age of 50 ± 1 Ma with a strong MSWD (14) and a clear excess argon component. For this sample a correlation between the different parts of the age spectrum and the $^{39}Ar/^{37}Ar$ (a proxy for the K/Ca ratio) is also visible (Table 1), suggesting a mixture of chemically different subgrains.

Table 2. The $^{40}Ar/^{39}Ar$ Analytical Data for K-Feldspars[a]

Temperature, °C	$^{40}Ar/^{39}Ar$	$^{38}Ar/^{39}Ar$	$^{37}Ar/^{39}Ar$	$^{36}Ar/^{39}Ar$ (10^{-3})	^{39}Ar, 10^{-14} mol	$F^{39}Ar$ Released	$\%^{40}Ar^*$	$^{40}Ar^*/^{39}Ar$	Age, Ma	$\pm1\sigma$, Ma
				NV1 K-Feldspar						
400	16.593	0.018	0.000	14.439	0.12	1.94	74.17	12.31	168.88	1.78
400	6.258	0.000	0.000	0.002	0.05	2.82	99.67	6.24	87.57	0.73
450	6.157	0.016	0.000	6.845	0.11	4.66	66.82	4.11	58.23	1.31
450	5.454	0.001	0.000	3.959	0.07	5.76	78.18	4.26	60.32	1.25
500	206.153	0.137	0.001	662.383	0.11	7.63	5.04	10.40	143.72	20.87
500	127.086	0.077	0.000	396.727	0.08	8.95	7.74	9.83	136.18	19.41
525	89.000	0.068	0.000	263.296	0.12	10.98	12.56	11.18	154.01	10.00
525	33.114	0.035	0.000	54.485	0.23	14.87	51.32	16.99	229.26	2.38
550	57.574	0.057	0.004	153.036	0.09	16.37	21.42	12.33	169.23	9.35
550	37.544	0.020	0.000	97.058	0.05	17.22	23.56	8.84	122.94	8.78
575	29.984	0.020	0.010	63.447	0.05	18.14	37.41	11.22	154.54	5.50
575	33.885	0.018	0.000	78.958	0.05	19.02	31.08	10.53	145.50	8.27
600	27.409	0.033	0.011	54.638	0.06	20.07	41.02	11.24	154.91	6.50
600	35.266	0.009	0.004	81.742	0.06	21.12	31.45	11.09	152.89	8.92
625	28.185	0.031	0.006	58.171	0.07	22.33	38.94	10.98	151.37	6.13
625	30.970	0.019	0.005	66.880	0.09	23.77	36.12	11.19	154.15	3.30
650	18.667	0.030	0.000	26.794	0.10	25.52	57.48	10.73	148.10	2.39
650	13.759	0.004	0.003	12.764	0.12	27.50	72.44	9.97	137.98	1.60
675	11.102	0.019	0.003	4.416	0.13	29.65	88.07	9.78	135.44	1.57
675	11.404	0.011	0.000	5.071	0.11	31.49	86.69	9.89	136.89	1.78
700	11.413	0.019	0.005	7.484	0.10	33.13	80.45	9.18	127.48	2.26
700	11.761	0.018	0.009	0.002	0.08	34.46	99.83	11.74	161.47	2.21
725	12.183	0.028	0.009	5.620	0.07	35.69	86.21	10.50	145.09	2.72
725	13.664	0.023	0.001	7.406	0.05	36.58	83.84	11.46	157.70	3.68
750	13.934	0.014	0.021	7.276	0.05	37.48	84.44	11.76	161.77	3.72
750	13.620	0.013	0.000	2.973	0.04	38.23	93.40	12.72	174.31	3.41
775	14.696	0.032	0.016	17.713	0.04	38.96	64.25	9.44	130.97	4.75
775	16.460	0.031	0.000	1.593	0.03	39.44	97.02	15.97	216.24	3.79
800	15.230	0.047	0.015	21.748	0.04	40.08	57.68	8.78	122.15	5.50
800	18.054	0.027	0.000	9.791	0.03	40.58	83.86	15.14	205.63	3.80
800	21.362	0.000	0.000	0.004	0.03	41.09	99.90	21.34	283.52	5.39
800	17.436	0.019	0.001	0.006	0.02	41.45	99.88	17.41	234.58	6.10
850	16.400	0.025	0.015	6.399	0.05	42.26	88.35	14.49	197.27	3.86
900	14.026	0.025	0.006	3.155	0.12	44.32	93.21	13.07	178.91	2.04
950	13.763	0.021	0.004	3.066	0.27	48.79	93.27	12.84	175.82	1.22
1000	14.430	0.019	0.002	1.800	0.43	56.05	96.18	13.88	189.35	0.78
1050	15.278	0.018	0.002	0.594	0.60	66.20	98.72	15.08	204.89	0.74
1100	15.312	0.019	0.020	0.484	0.82	80.02	98.94	15.15	205.76	0.71
1200	14.749	0.018	0.001	0.638	1.14	99.26	98.59	14.54	197.92	0.57
1400	21.040	0.000	0.000	23.028	0.04	100.00	67.56	14.22	193.72	6.88
				NV7 K-Feldspar						
400	6.278	0.021	0.004	6.432	1.14	2.95	69.41	4.36	61.63	0.29
400	2.114	0.012	0.003	0.887	0.75	4.92	86.67	1.83	26.16	0.32
450	2.251	0.013	0.003	1.045	1.55	8.96	85.40	1.92	27.44	0.15
450	2.193	0.012	0.002	0.700	1.03	11.63	89.67	1.97	28.07	0.16
500	31.432	0.032	0.003	96.576	1.51	15.57	9.14	2.87	40.88	1.78
500	6.584	0.015	0.004	14.765	0.88	17.86	33.43	2.20	31.39	0.42
550	5.381	0.015	0.004	9.991	1.37	21.42	44.77	2.41	34.32	0.29
550	3.785	0.016	0.017	2.183	1.05	24.13	82.46	3.12	44.35	0.24
600	3.807	0.018	0.005	1.845	1.42	27.82	85.16	3.24	46.05	0.22
600	3.824	0.017	0.006	1.270	0.78	29.84	89.67	3.43	48.67	0.32
650	3.535	0.015	0.006	1.725	0.65	31.54	85.03	3.01	42.73	0.41
650	3.782	0.017	0.006	1.664	0.55	32.98	86.48	3.27	46.45	0.41
700	4.184	0.016	0.005	3.649	0.72	34.84	73.75	3.09	43.85	0.34
700	4.181	0.016	0.004	2.320	0.60	36.40	83.13	3.48	49.32	0.37
750	4.612	0.017	0.004	4.901	0.76	38.37	68.17	3.14	44.67	0.33
750	5.014	0.018	0.004	5.831	0.63	40.01	65.24	3.27	46.45	0.34
800	5.036	0.017	0.004	6.424	0.84	42.20	61.92	3.12	44.31	0.35
800	4.932	0.016	0.004	6.341	0.88	44.49	61.61	3.04	43.19	0.35
800	3.763	0.015	0.003	2.230	1.19	47.57	81.96	3.08	43.84	0.24
800	3.509	0.015	0.004	1.727	0.62	49.17	84.89	2.98	42.34	0.29
850	3.475	0.016	0.004	1.091	0.80	51.24	90.15	3.13	44.51	0.26
900	3.369	0.015	0.004	1.157	1.25	54.49	89.26	3.01	42.75	0.21
950	3.366	0.016	0.003	1.127	1.61	58.69	89.52	3.01	42.84	0.18
1000	3.757	0.017	0.003	1.260	1.90	63.62	89.56	3.36	47.76	0.19
1050	4.163	0.018	0.003	1.557	2.47	70.04	88.47	3.68	52.22	0.20
1100	4.224	0.017	0.002	1.361	3.89	80.16	90.01	3.80	53.88	0.19

Table 2. (continued)

Temperature, °C	$^{40}Ar/^{39}Ar$	$^{38}Ar/^{39}Ar$	$^{37}Ar/^{39}Ar$	$^{36}Ar/^{39}Ar$ (10^{-3})	^{39}Ar, 10^{-14} mol	$F^{39}Ar$ Released	$\%^{40}Ar^*$	$^{40}Ar^*/^{39}Ar$	Age, Ma	$\pm1\sigma$, Ma
1200	5.163	0.017	0.001	3.991	7.00	98.36	76.78	3.96	56.14	0.22
1400	8.279	0.020	0.007	12.340	0.63	100.00	55.72	4.61	65.17	0.50
					BS1 K-Feldspar					
400	40.247	0.092	0.002	10.869	0.83	3.04	91.97	37.02	466.59	1.13
400	7.817	0.023	0.002	3.566	0.20	3.78	86.26	6.74	94.49	0.65
450	16.900	0.050	0.005	4.756	0.40	5.23	91.57	15.48	209.92	0.81
450	6.095	0.019	0.004	3.167	0.12	5.68	84.32	5.14	72.46	0.66
500	335.288	0.235	0.003	1063.619	0.14	6.19	6.25	20.97	278.94	27.03
500	36.353	0.044	0.005	92.856	0.09	6.51	24.47	8.89	123.62	3.24
525	21.777	0.039	0.006	38.884	0.16	7.08	47.15	10.27	141.96	1.71
525	14.713	0.042	0.002	6.983	0.30	8.18	85.84	12.63	173.11	0.89
550	14.471	0.043	0.002	5.153	0.51	10.05	89.34	12.93	177.01	0.74
550	14.463	0.041	0.002	2.796	0.58	12.15	94.15	13.62	185.96	0.59
575	14.691	0.042	0.002	2.641	0.46	13.83	94.55	13.89	189.52	0.65
575	14.196	0.040	0.002	2.555	0.35	15.10	94.54	13.42	183.42	0.74
600	13.712	0.040	0.003	3.474	0.30	16.20	92.37	12.67	173.58	0.86
600	13.786	0.040	0.003	2.292	0.27	17.19	94.94	13.09	179.10	0.84
625	13.197	0.039	0.000	3.295	0.22	17.99	92.47	12.20	167.53	0.86
625	13.143	0.044	0.004	3.014	0.22	18.79	93.07	12.23	167.91	0.73
650	13.308	0.040	0.001	4.200	0.20	19.51	90.52	12.05	165.48	0.86
650	13.272	0.039	0.000	3.140	0.20	20.25	92.86	12.32	169.11	0.86
675	13.525	0.040	0.003	5.110	0.22	21.05	88.69	11.99	164.79	0.91
675	13.268	0.040	0.000	3.543	0.24	21.92	91.96	12.20	167.50	0.82
700	13.722	0.039	0.003	6.098	0.25	22.82	86.72	11.90	163.55	0.90
700	13.507	0.039	0.003	4.532	0.28	23.86	89.94	12.15	166.81	0.88
725	13.582	0.039	0.004	6.441	0.30	24.96	85.84	11.66	160.38	0.81
725	13.176	0.040	0.003	5.187	0.32	26.14	88.22	11.62	159.91	0.80
750	22.113	0.031	0.002	36.979	0.91	29.46	50.49	11.17	153.88	0.94
750	12.114	0.024	0.002	2.204	0.59	31.64	94.46	11.44	157.53	0.52
775	12.798	0.025	0.002	2.725	0.50	33.45	93.55	11.97	164.51	0.58
775	12.810	0.028	0.003	4.076	0.27	34.45	90.44	11.59	159.41	0.81
800	13.191	0.030	0.005	4.528	0.28	35.47	89.71	11.83	162.68	0.88
800	12.337	0.031	0.003	4.101	0.22	36.29	90.02	11.11	153.08	0.84
800	11.915	0.026	0.001	1.691	0.22	37.10	95.64	11.40	156.91	0.62
700	12.670	0.012	0.000	0.003	0.04	37.26	99.84	12.65	173.37	1.13
750	12.387	0.028	0.012	0.573	0.05	37.45	98.48	12.20	167.46	1.28
800	12.789	0.031	0.000	3.540	0.15	38.01	91.66	11.72	161.22	0.92
850	14.588	0.034	0.003	3.291	0.31	39.13	93.20	13.60	185.69	0.71
900	13.582	0.034	0.002	3.544	0.56	41.17	92.14	12.52	171.61	0.60
950	13.667	0.034	0.003	3.029	1.12	45.24	93.31	12.75	174.71	0.60
1000	14.127	0.034	0.002	2.378	2.19	53.26	94.88	13.40	183.20	0.69
1050	13.798	0.033	0.001	1.686	4.89	71.15	96.25	13.28	181.58	0.73
1100	13.556	0.032	0.001	1.386	6.22	93.90	96.83	13.13	179.59	0.50
1200	14.169	0.034	0.002	2.417	1.59	99.71	94.82	13.44	183.61	0.48
1400	30.347	0.058	0.018	42.591	0.08	100.00	58.47	17.74	238.73	3.95
					BS7 K−Feldspar					
400	20.394	0.040	0.000	33.724	0.12	5.63	51.04	10.41	143.85	2.14
400	6.935	0.000	0.000	2.493	0.04	7.53	89.09	6.18	86.75	1.32
450	12.045	0.013	0.001	10.844	0.05	10.01	73.23	8.82	122.62	2.10
450	12.919	0.000	0.000	6.171	0.02	11.12	85.73	11.08	152.69	4.01
500	1185.431	0.733	0.009	3793.218	0.05	13.28	5.44	64.52	748.79	275.08
500	34.467	0.017	0.000	37.118	0.08	16.89	68.12	23.48	309.60	3.55
525	26.181	0.028	0.002	10.825	0.23	27.91	87.71	22.96	303.34	1.40
525	29.268	0.027	0.002	21.445	0.15	34.83	78.28	22.91	302.71	2.12
550	49.236	0.034	0.010	85.833	0.06	37.66	48.45	23.85	314.13	6.68
550	36.477	0.017	0.000	40.371	0.02	38.48	67.24	24.53	322.27	14.31
575	31.622	0.005	0.032	27.713	0.02	39.39	74.05	23.42	308.84	11.59
575	25.892	0.008	0.001	17.515	0.02	40.47	79.93	20.70	275.57	7.71
600	29.486	0.013	0.010	35.427	0.03	41.82	64.43	19.00	254.48	9.11
600	34.925	0.000	0.000	54.190	0.03	43.21	54.09	18.89	253.16	9.79
625	45.479	0.025	0.029	90.964	0.03	44.39	40.86	18.58	249.26	14.61
625	38.523	0.000	0.002	62.097	0.03	45.68	52.32	20.15	268.85	12.16
650	34.600	0.017	0.008	48.716	0.03	47.04	58.34	20.19	269.25	9.87
650	33.373	0.004	0.005	56.952	0.04	48.71	49.51	16.52	223.30	8.25
675	30.368	0.023	0.007	50.480	0.06	51.32	50.82	15.43	209.37	6.27
675	25.834	0.008	0.000	29.601	0.06	54.05	66.06	17.07	230.19	4.74
700	23.200	0.024	0.007	23.702	0.08	57.68	69.73	16.18	218.89	3.44

Table 2. (continued)

Temperature, °C	$^{40}Ar/^{39}Ar$	$^{38}Ar/^{39}Ar$	$^{37}Ar/^{39}Ar$	$^{36}Ar/^{39}Ar$ (10^{-3})	^{39}Ar, 10^{-14} mol	$F^{39}Ar$ Released	$\%^{40}Ar^*$	$^{40}Ar^*/^{39}Ar$	Age, Ma	$\pm1\sigma$, Ma
700	24.270	0.016	0.004	26.705	0.09	62.03	67.40	16.36	221.20	2.48
725	25.532	0.022	0.006	36.300	0.12	67.93	57.91	14.79	201.07	2.81
725	23.300	0.018	0.000	27.169	0.12	73.55	65.46	15.25	207.05	2.38
750	16.063	0.017	0.009	6.858	0.08	77.55	87.26	14.02	191.15	2.28
750	17.861	0.019	0.000	4.223	0.05	79.91	92.90	16.59	224.18	3.34
775	19.310	0.027	0.011	9.818	0.04	81.70	84.87	16.39	221.59	3.99
775	21.777	0.007	0.000	10.600	0.02	82.74	85.53	18.63	249.81	7.40
800	24.156	0.066	0.016	32.530	0.02	83.67	60.13	14.52	197.70	10.46
800	27.635	0.021	0.000	21.600	0.01	84.35	76.83	21.23	282.17	15.28
800	37.702	0.000	0.000	0.014	0.01	84.78	99.94	37.68	473.94	8.14
900	27.605	0.049	0.010	47.650	0.02	85.88	48.92	13.50	184.51	9.39
950	28.541	0.024	0.017	43.246	0.03	87.23	55.16	15.74	213.35	7.62
1000	24.455	0.036	0.000	28.296	0.04	89.17	65.73	16.07	217.56	5.57
1050	22.347	0.017	0.011	10.525	0.06	91.83	86.00	19.22	257.22	4.19
1100	20.262	0.023	0.011	5.455	0.09	95.89	91.95	18.63	249.89	2.41
1200	20.263	0.011	0.001	8.224	0.08	99.54	87.91	17.81	239.62	3.27
1400	45.826	0.000	0.078	68.784	0.01	100.00	55.61	25.49	333.77	25.17

[a] J = 0.007974.

3.4. The $^{40}Ar/^{39}Ar$ Interpretation

[11] Laser probe $^{40}Ar/^{39}Ar$ step-heating of biotite single grains reveals only partial resetting of the late Variscan micas during the Pyrenean orogeny, which suggests that temperature never exceeded 300–350°C in the two studied massifs. This resetting is more pronounced in the Néouvielle massif than in the Bielsa massif, which probably results from a deeper burial or a longer residence at depth of the former compared to the latter. It is noteworthy that, by contrast with the fission track results (see below), biotite ages are older in the core of the two massifs, which suggests some inclination of isotherms during the tectonic burial of these two massifs.

[12] With the exception of sample NV7, $^{40}Ar/^{39}Ar$ step heating of K-feldspar bulk separates also indicates partial isotopic resetting with total ages ranging from 202 to 284 Ma. The age spectra are strongly discordant but do not display typical profiles of argon loss similar to those modeled by *Lovera et al.* [1989, 1991]. This results from the interaction of argon loss by volume diffusion and incorporation of fluids with a high $^{40}Ar/^{39}Ar$ initial ratio producing ages older than what we could have expected from a mineral thermally overprinted during the Pyrenean orogeny [*Henderson and McCaig*, 1996; *Ingles et al.*, 1999]. It was not possible to correct for excess argon following the method proposed by *Harrison et al.* [1994], suggesting that initial $^{40}Ar/^{36}Ar$ ratio of excess argon was not homogeneous, either from fluid heterogeneity, interaction with multiple fluids or repeated interaction with fluid in time. The only sample showing resetting is sample NV7 for which we observed in thin section an overgrowth of newly formed K-feldspar around the magmatic Variscan K-feldspar, suggesting fluid circulation within the granite during the Pyrenean orogeny [*Henderson and McCaig*, 1996; *Ingles et al.*, 1999]. This sample has been nearly totally reset during the early Eocene, which contrasts with the isotopic behavior of coexisting biotite at 236 Ma, despite the fact that biotite and the most retentive domains of K-feldspar degassed at high experimental temperature have a relatively similar closure temperature of 250–300°C. Most probably this results from the fact that the biotite selected for dating was the best preserved grain among a mica population showing strong chloritization effects due to the fluid impregnation. Unfortunately heterogeneous excess argon and feldspar overgrowth prohibits the use of thermal modeling as developed by *Lovera et al.* [1991].The occurrence and role of fluid circulation in the Néouvielle massif during the Pyrenean orogeny will be developed further in the discussion.

3.5. Apatite Fission Tracks Methodology

[13] Eight samples were selected for apatite fission track analysis. The apatite grains were mounted on glass slides using epoxy glue and polished. Samples were etched in 6.5% HNO_3 for 45 s at 20°C to reveal the spontaneous fission tracks, before being irradiated with a neutron flux of $1.0 \times 10_{16}$ neutrons cm^{-2} (ANSTO, Lucas Height, Australia). The micas used as external detector were etched in 40% HF for 40 min at 20°C in order to reveal the induced fission tracks. The ages were calculated following the method recommended by the Fission Track Working Group of the IUGS Subcommission on Geochronology [*Hurford*, 1990] using the zeta calibration method [*Hurford and Green*, 1983] and the Trackkey software (Dunkl, University of Tuebingen). CN5 glass was used as dosimeter with a zeta value of 340 ± 6 (M. Campani), obtained on Durango apatite standards. Fission tracks were counted on a Zeiss microscope, using a magnification of 1250 under dry objectives. Because all samples passed the χ^2 test, ages given in the text are central ages and errors are quoted at $\pm2\sigma$.

[14] To better constrain the age of thermal events, inverse modeling of track lengths distribution has been performed using the AFTSolve software [*Ketcham et al.*, 2000] and the *Ketcham et al.* [1999] annealing model (Figure 6). Anneal-

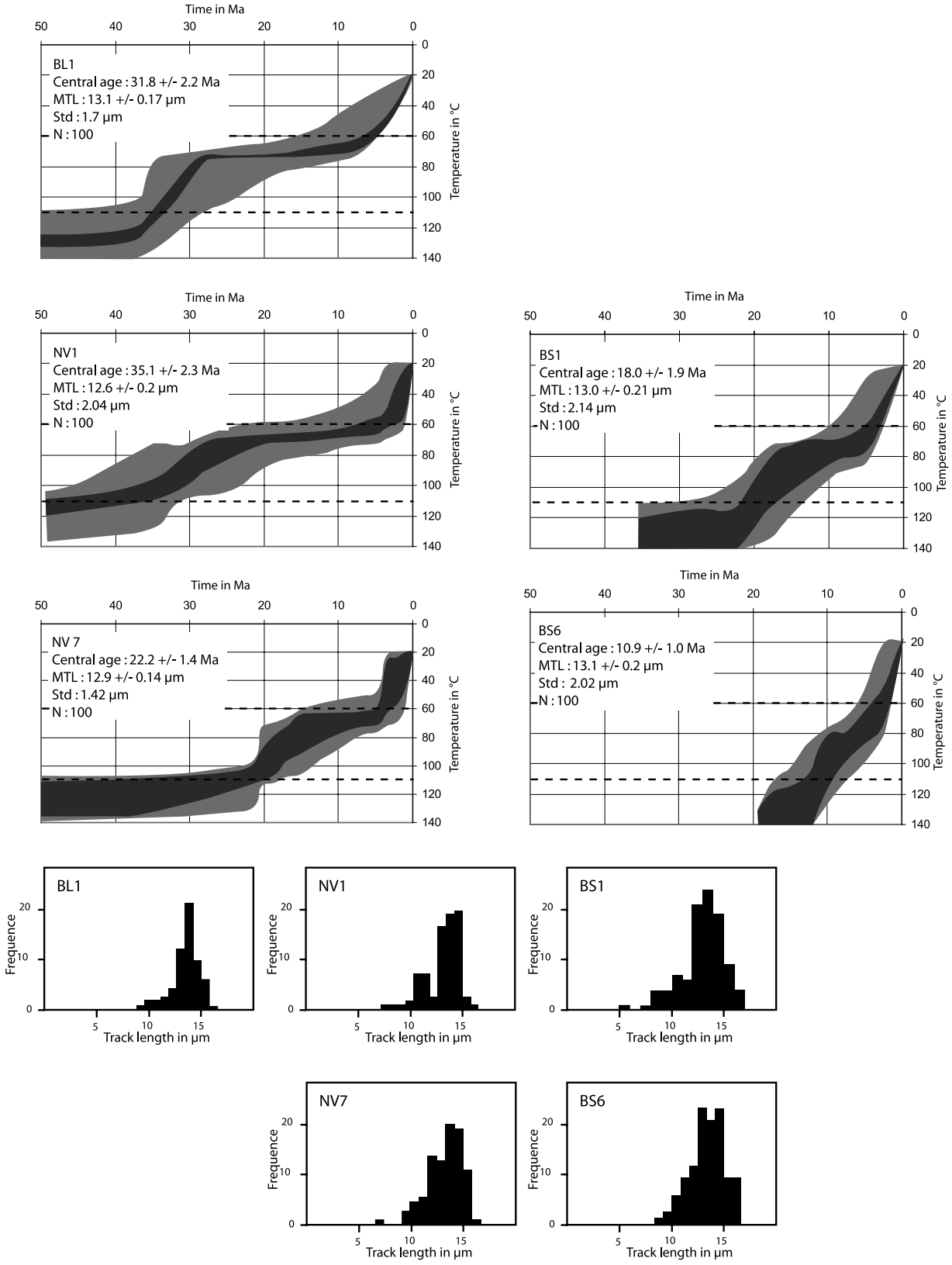
Time in Ma
50 40 30 20 10 0
0 20 40 60 80 100 120 140
Temperature in °C
BL1
Central age : 31.8 +/- 2.2 Ma
MTL : 13.1 +/- 0.17 µm
Std : 1.7 µm
N : 100
NV1
Central age : 35.1 +/- 2.3 Ma
MTL : 12.6 +/- 0.2 µm
Std : 2.04 µm
N : 100
BS1
Central age : 18.0 +/- 1.9 Ma
MTL : 13.0 +/- 0.21 µm
Std : 2.14 µm
N : 100
NV 7
Central age : 22.2 +/- 1.4 Ma
MTL : 12.9 +/- 0.14 µm
Std : 1.42 µm
N : 100
BS6
Central age : 10.9 +/- 1.0 Ma
MTL : 13.1 +/- 0.2 µm
Std : 2.02 µm
N : 100
Frequence
0 10 20
5 10 15
Track length in µm
BL1
NV1
BS1
NV7
BS6

Figure 6

Table 3. Apatite Fission Track Analytical Data[a]

Sample	Altitude, m	Mineral	Number of Grains	Standard Track Density, $\times 10^4$ cm^{-2} (Counted)	ρ_S, $\times 10^4$ cm^{-2} (Counted)	ρ_i, $\times 10^4$ cm^{-2} (Counted)	U Concentration, ppm	P(χ^2), %	Var, %	Mean Track Length ± 1σ, μm (Counted)	Dpar, μm	Central Age ± 2σ, Ma
NV1	3100	Ap	20	162.8 (14699)	46.3 (302)	365.6 (2373)	26.1	89.92	2.2	12.6 ± 0.2 (100)	1.96	35.1 ± 2.3
NV7	1900	Ap	20	153.3 (14699)	44.6 (289)	522.5 (3386)	41.07	75.8	0.4	12.9 ± 0.14 (100)	2.01	22.2 ± 1.4
NV13	2100	Ap	20	143.8 (14699)	31.8 (213)	283.1 (1894)	23.37	75.3	0.2	—	1.98	27.5 ± 2.1
BL1	900	Ap	20	166 (14699)	48.9 (267)	433.9 (2365)	31.32	38.6	0.6	13.1 ± 0.17 (100)	2.21	31.8 ± 2.2
PE2	1800	Ap	19	140.7 (14699)	26.2 (74)	293.6 (828)	21.15	64.65	2.3	—	2.15	23.5 ± 2.7
BS1	2600	Ap	20	131.2 (14699)	19.3 (163)	238.7 (2015)	23.17	45.53	0.3	13.0 ± 2.1 (100)	2.05	18.0 ± 1.9
BS6	1400	Ap	20	124.9 (14699)	37.8 (123)	736.3 (2393)	65.75	94.27	2.8	13.1 ± 2.0 (100)	2.15	10.9 ± 1.0
BS7	1100	Ap	11	130.5 (11732)	31.2 (56)	356.9 (639)	32.14	71.37	0	—	2.20	19.4 ± 2.7

[a]Ap, apatite; ρ_S and ρ_i represent sample spontaneous and induced track densities; P(χ^2) is the probability of χ^2 for v degrees of freedom (where v is number of crystals minus 1).

ing kinetics of fission tracks in apatite is strongly dependent on the chemical composition of the mineral (variations in concentration of elements such as Cl and F, for example). The resistance to annealing of an apatite crystal due to its chemical composition can be estimated using the Dpar parameter (length of the etch pit parallel to the *c* crystallographic axis) [*Donelick*, 1993; *Burtner et al.*, 1994; *Barbarand et al.*, 2003]. Dpar values obtained for each sample were used as input parameters in the AFTSolve models.

3.6. Apatite Fission Tracks Results

[15] Within the Néouvielle massif (and considering sample PE2 as part of the massif), central ages vary from 22.2 ± 1.4 Ma to 35.1 ± 2.3 Ma (Figure 3). Only the NV1 and NV7 samples displayed enough horizontal fission tracks to calculate the mean fission track lengths (MTL), with values of 12.6 ± 0.2 μm and 12.9 ± 0.14 μm, respectively (Table 3). Dpar values vary between 1.96 and 2.15 μm. There is an apparent age-altitude correlation, with all the samples that were collected on the 2000 m high horizontal profile having a central age between 22 and 27 Ma, whereas sample NV1 that was collected at the top of the massif (3100 m) is much older (35 Ma) (Figure 3). Sample BL1 (900 m) from the Bordère-Louron massif gives an age of 31.8 ± 2.2 Ma and a MTL of 13.1 ± 0.17 for a Dpar of 2.21 μm.

[16] The age-altitude correlation also exists in the Bielsa massif between the summit sample BS1 (2600 m) and sample BS6 in the core of the massif (1400 m), which yield central ages of 18.0 ± 1.9 Ma and 10.9 ± 1.0 Ma, respectively (Figure 3). By contrast, samples BS1 and BS7 (1100 m), both close to the post-Variscan erosional surface, have approximately the same central age (19.4 ± 2.7 Ma for BS7) although their altitude difference is greater than between BS1 and BS6. Samples BS1 and BS6 have MTL of 13.0 ± 0.21 and 13.1 ± 0.2 μm; MTL was not calculated for sample BS7 due to the very small number of horizontal fission tracks. Dpar values vary from 2.05 to 2.20 μm.

3.7. Apatite Fission Track Interpretation

[17] Fission track data show that sample NV1 from the top of the Néouvielle massif cooled through the 110°C isotherm between circa 45 and 35 Ma with a cooling rate of 3°C Ma^{-1} (Figure 6). This first cooling episode stopped around 70°C and was followed by a period of very slow cooling. Final cooling happened after 5 Ma. The base of the Néouvielle (NV7) crossed the 110°C isotherm much later, around 20 Ma and kept cooling until 15 to 13 Ma. Then, it recorded a similar evolution as NV1 with nearly stopped cooling around 70°C and a final exhumation around 5 Ma.

Figure 6. Reverse modeling of apatite fission track lengths for samples BL1, NV1, NV7, BS1, and BS6 obtained using the AFTSolve® software. The fission track central age is reported on the graph as well as the measured mean track length (MTL) and the number of tracks measured (N). The dark grey area represents the envelope of all the possible temperature-time curves falling within a 1σ error interval from the best fit curve. The light grey area represents the envelope of all the cooling curves falling within a 2σ interval. Only the area between 110°C and 60°C (designed as partial annealing zone or PAZ) is representative. The track lengths histogram is displayed for each sample. See text for discussion of the graphs.

Sample BL1 shows the same cooling history as NV1. Sample from the top of the Bielsa granite (BS1) crossed the 110°C isotherm between 22 and 17 Ma with a cooling rate of 3°C Ma^{-1} similar to the first cooling episode in the Néouvielle massif (Figure 6). Then, from circa 15 Ma cooling nearly stopped and temperature stayed around 70°C until circa 5 Ma when the Bielsa massif was affected by a cooling event similar in time and rate to the last event in the Néouvielle massif. Timing of the cooling history of sample BS6, in the core of the Bielsa granite, is different as the first cooling event initiated around 12 to 10 Ma and passed almost continuously to the final cooling around 5 Ma.

4. Discussion

4.1. Burial History of the Granite Massifs

[18] Except for the NV7 sample, $^{40}Ar/^{39}Ar$ data on biotite and K-feldspar present intermediate ages between the Hercynian and Pyrenean deformation episodes, which thus cannot be interpreted as cooling ages. This suggests that after the post-Hercynian erosion, temperature never exceeded about 300°C in the two massifs, the temperature required for a major argon resetting in the two chronometers. Considering a normal geothermal gradient, this would indicate that the maximum burial depth of the two massifs before and during the Pyrenean orogeny was less than 10 km, most probably in the range 6–8 km. The $^{40}Ar/^{39}Ar$ thermochronological data also suggest that the more internal Néouvielle massif was buried deeper than the external Bielsa one.

[19] The $^{40}Ar/^{39}Ar$ dating of NV7 K-feldspar provides a complex age spectrum with total age of circa 53 Ma that contrasts with the 236 Ma biotite age from the same sample. NV7 was sampled at a few tens of meters from one of the mylonite corridors belonging to the eastern termination of the Eaux-Chaudes thrust. A Rb-Sr age of 48 ± 2 Ma obtained by *Wayne and McCaig* [1998] on mylonite veins (whole rock and vein minerals: amphibole, epidote, calcite, and albite) confirms the occurrence of Pyrenean movements along those shear zones. Petrographic observations indicate that important fluid circulation occurred within the mylonite corridors [*Henderson and McCaig*, 1996] with temperatures of 300 to 350°C deduced from fluid inclusions and petrography [*Henderson and McCaig*, 1996; *Ingles et al.*, 1999; M. Campani, unpublished data, 2005]. In NV7 sample, it is likely that K-feldspar overgrowths formed around the magmatic K-feldspar are coeval with this fluid activity as suggested by the pseudoplateau age of about 50 Ma obtained at intermediate temperature (Figure 5). This reinforces the idea of tectonic activity along the mylonitic zones that form the eastern termination of the Eaux-Chaudes thrust and thus early Eocene activity along the thrust itself. Younger ages would reflect cooling of these overgrowths and older ones, inherited argon in the magmatic K-feldspar core. The fluid activity in this sample is also attested by the advanced chloritization of the biotite population, the dated grain at 236 Ma being one of the less affected by this process, thus having best preserved its Hercynian argon signature.

[20] Fission track ages indicate that all the samples have been exhumed from temperatures higher than 110°C during the Pyrenean episode. Considering a geothermal gradient of 25 to 30°C km^{-1}, the granite massifs were thus buried, before circa 35 Ma for Néouvielle and Bordère-Louron, and circa 20 Ma for Bielsa to depths of at least 4 km (below the fission track annealing zone) and likely less than 6–8 km as suggested by $^{40}Ar/^{39}Ar$ thermochronological data, depending on the considered massif.

[21] Except thin local remnants of Permian sediments, the Bielsa massif is directly covered by Upper Cretaceous limestones. The sedimentary cover of the Néouvielle is unknown due to erosion, but farther west, the Balaïtous granite which has the same altitude and structural position as the Néouvielle massif, is also capped by Upper Cretaceous limestones. We thus assume that both the Néouvielle and Bielsa massifs were at, or close to, the surface before the Late Cretaceous transgression, and were then covered by a sedimentary succession similar to that presently preserved along the southern border of, and above the western termination of, the Axial Zone (Figure 3). This implies ~1000 m of Upper Cretaceous–Paleocene shelf deposits, followed by the lower part of the lower Eocene turbidite succession, that corresponds to the first stages of subsidence of the south Pyrenean foredeep [*Labaume et al.*, 1985; *Teixell*, 1996]. Although the original thickness of these turbidites is not known, it probably not exceeded 2000 to 3000 m. The sedimentary burial of the granite massifs may have thus been close to, or even reached, the 3–4 km necessary for the reset of the apatite fission track system as a result of the overlying foredeep fill. Sedimentary burial was then followed by tectonic burial when the deformation front propagated southward, thus leading the granites to their maximum temperature during the Pyrenean orogenic cycle (Figure 7). On the basis of the tectonic-sedimentation relationships in the Jaca and Ainsa basins, this probably occurred during the early middle Eocene for the Néouvielle massif (emplacement of the Eaux-Chaudes thrust, passing southward to the Monte Perdido thrust in the Jaca and Ainsa basins) and the late Eocene–early Oligocene for the Bielsa massif (emplacement of the Gavarnie thrust) [*Labaume et al.*, 1985; *Teixell*, 1996].

4.2. Exhumation History of the Granite Massifs

[22] Both central fission track ages and track lengths modeling of summit samples NV1 and BS1 indicate that the Néouvielle massif has been exhumed prior to the Bielsa massif.

[23] In the Néouvielle massif, sample NV1 crossed the 110°C isotherm around 35 Ma which is consistent with a late Eocene age of activity on the Gavarnie thrust. Cooling of sample NV1 stopped around 25 to 20 Ma suggesting that the Gavarnie thrust was not active anymore.

[24] Samples NV13, NV7, and PE2, as well as sample LA7 from *Morris et al.* [1998], were collected along a mostly horizontal profile around 2000 m of elevation and

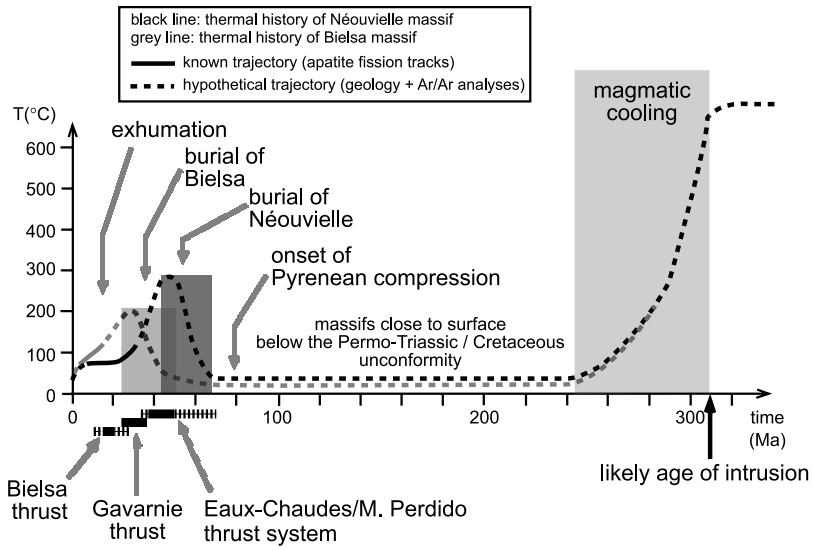

Figure 7. Thermal history of the Néouvielle and Bielsa granites.

parallel to the direction of compression. These samples display, within the error margins, the same central fission track age of about 25 ± 2 Ma. The Néouvielle massif thus appears to have been exhumed as a single, rigid block on the hanging wall of the Gavarnie thrust. Sample PE2, in the footwall of the Pic-Long thrust does not reveal any major movement on that fault during or after the exhumation of the massif indicating that this fault was active before circa 30 Ma but did not participate to the exhumation of the Néouvielle massif. Furthermore, there is no indication of tilting of the massif during its exhumation.

[25] The central age of 31.8 ± 2.2 Ma obtained for sample BL1 in the Bordère-Louron granite (close to the 35.0 ± 2.8 Ma age obtained by *Morris et al.* [1998] on the same massif) is more difficult to explain. This age is close to the 35.1 ± 2.3 Ma obtained for sample NV1 situated 2200 m higher in the Néouvielle massif. Furthermore, the thermal histories derived from fission track lengths modeling of both samples are similar, implying that they have been exhumed at the same time and in the same way between 110 and 60°C. Differential exhumation probably not happened after 5 Ma (outside of the apatite partial annealing zone) because (1) there is no evidence of a major fault between the two granites that could explain similar ages at very different altitudes, and (2) by that time the tectonic activity in the Axial Zone had stopped. The favored hypothesis is the occurrence at depth of an east dipping lateral footwall ramp of the Gavarnie thrust, subparallel to the direction of movement, and located between the Néouvielle and Bordère-Louron massifs. This resulted in thrusting of the Néouvielle massif higher than the Bodère-Louron massif, inducing folding and tilting of the isotherms following a paleotopography inclined toward the east above the lateral ramp. This resulted in a similar cooling path for samples NV1 and BL1 not correlated to their difference in altitude.

[26] Samples NV1 and NV7 from the Néouvielle subvertical profile show relatively discordant thermal histories. NV7 entered the PAZ at the end of the initial cooling episode of NV1 which is consistent with its position deeper in the crust. However, while NV1 reached the very slow cooling stage, NV7 keep cooling at a higher rate until circa 15 Ma when its thermal history can be superimposed to the one of NV1. One possible explanation for this discrepancy between the two thermal histories could be the formation through erosion between 20 and 15 Ma of a paleovalley similar to the actual one. Localized erosion above sample NV7 would have induced cooling of sample NV7 compared to a stable NV1. Vertical incision rates would have been of the order of 0.1 mm yr^{-1}, similar to the Miocene and Quaternary incision rates reported by *Vergés et al.* [2002] farther east.

[27] In the Bielsa massif, samples BS1 and BS7 with their central fission track ages of 18 ± 1.9 and 19.4 ± 2.7 Ma, respectively, imply that the Bielsa massif was first uplifted vertically before being tilted southward between 18 and 11 Ma when BS6 (in the core of the massif) was exhumed. The sample BA3 from *Morris et al.* [1998], at an elevation of 1020 m and also located at the top of the granite (Figure 3), yielded a central age of 16.0 ± 1.5 Ma consistent with this interpretation. *Casas et al.* [2003] showed that the Bielsa granite was deformed by folding during its exhumation when passing above a footwall ramp of the Bielsa thrust. Two scenarios can explain the relationship between exhumation of the granite and the formation of this hanging wall ramp anticline: a) from circa 22 to 17 Ma (Figure 6), the Bielsa massif was exhumed without tilting or folding along the ramp of the Bielsa thrust. Subsequently folding and thus tilting of the post-Variscan surface occurred when the granite body passed from above the ramp to the footwall flat; b) the initial exhumation was driven by the more external Guarga thrust (Figure 2) and later, out-of-sequence movement

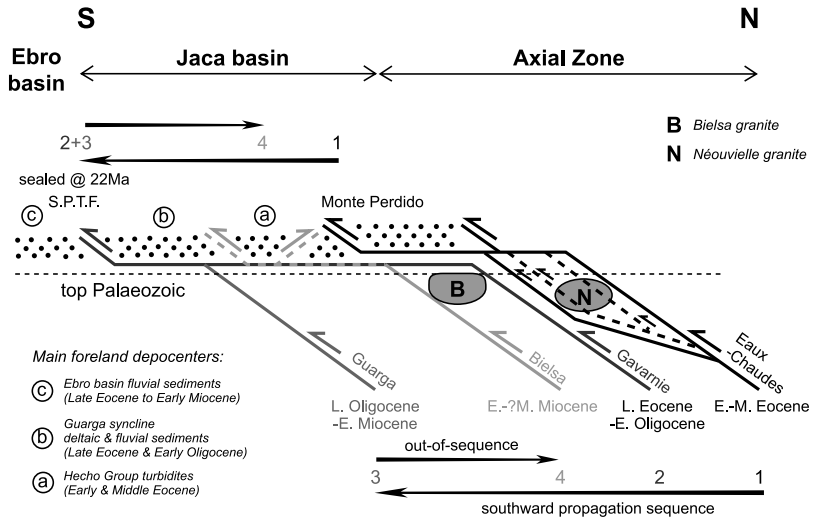

Figure 8. Summary of thrust sequence, derived from thermochronologic and geologic data.

along the Bielsa thrust induced folding and tilting. The second hypothesis implies that movement on the Guarga thrust continued until the Burdigalian, as it was proposed by some authors [e.g., *Millán Garrido et al.*, 2000] but is not confirmed by the dating of synorogenic sediments (see discussion below). On the other hand, we rule out the possibility that the similar ages obtained along the tilted top surface of the granite may result from posttilting (i.e., post-thrust) cooling across inclined isotherms. Indeed, this would imply that isotherms inclination was of the same order as the tilting of the granite top surface, i.e., a value of 35–40° unlikely at a 3.5–4 km depth.

[28] Finally, the last cooling event around 5 Ma recorded by sample NV7 from Néouvielle is also well expressed in sample BS1 from the Bielsa massif and could also be recorded in sample BL1 from Bordère-Louron although in this last sample it is much less constrained and will not be discussed further (Figure 6). Because it can be related to other geochronological and geological data that are discussed below, we cannot consider that this last cooling corresponds to the widely recognized artifact in modeling (the "late Miocene" cooling) generally associated with the use of the *Laslett et al.* [1987] annealing model [e.g., *Dempster and Persano*, 2006].

[29] The present morphology of the Pyrenees is characterized by the occurrence within the Axial Zone of remnants of high-elevation, low-relief erosion surfaces [*Babault et al.*, 2005]. When, by late Eocene, the Ebro basin became endoreic [e.g., *Vergés et al.*, 2002] it was filled by Oligo-Miocene continental deposits up to about 1000 m thicker than the presently preserved succession and that onlapped the southern edge of the Axial Zone [e.g., *Babault et al.*, 2005, and references therein]. Many authors proposed that reexcavation of the southern Pyrenees and Ebro basin was induced by the capture of the Ebro river by the Mediterranean Sea through a combination of the Miocene extensional tectonics within the Catalan chain and the Messinian desiccation crisis [e.g., *Nelson and Maldonado*, 1990; *Coney et al.*, 1996; *Garcia-Castellanos et al.*, 2003]. Using forward modeling of apatite fission track analysis data from the Maladeta massif, *Fitzgerald et al.* [1999] described a final cooling event starting between 10 and 5 Ma with a magnitude corresponding to a total denudation of 2 to 3 km. They relate this cooling to reexcavation of the southern Pyrenees by a proto-Ebro river during the Messinian. However, recent work by *Babault* [2004] and *Babault et al.* [2005] pointed out that the Miocene sediment accumulation and recent reexcavation also occurred on the northern flank of the belt. Considering that the base level of a chain is set by the river capacity to transport sediments, they defined the "efficient" base level of a chain as "the limit of the most proximal, extensive detrital sedimentation" and proposed that the recent lowering of this efficient base level, responsible for the reexcavation of both flanks of the belt, was due to the frequent and abrupt variations in climate since the Pliocene [*Babault et al.*, 2005].

[30] The last cooling event observed in our samples corresponds in age with the final cooling event observed by *Fitzgerald et al.* [1999] in the Maladeta and can reasonably be attributed to erosion during reexcavation of both the northern (Néouvielle and Bordère-Louron massifs) and southern (Bielsa massif) flanks of the Pyrenees. However, our data set is too small to discuss the differences between the models presented above.

4.3. Implications for the South Pyrenean Wedge Propagation

[31] The combination of our results with geological data is thus consistent with the propagation of basement thrusts toward the south from the Eaux-Chaudes thrust during the early middle Eocene to the Gavarnie thrust during the late Eocene–early Oligocene and the Guarga thrust during the late Oligocene–early Miocene (Figure 8). This propagation

caused the migration of the depocenters in the basin. The Hecho Group turbidites were deposited in the foreland of the Eaux-Chaudes thrust during the early middle Eocene and were affected by deformation when movement on the Eaux-Chaudes thrust propagated in decollement levels within cover sediments, resulting in the emplacement of the Monte Perdido thrust during the late Lutetian-Bartonian [*Labaume et al.*, 1985; *Teixell*, 1996]. When the Gavarnie thrust was activated, deformation and uplifting of the turbidite succession continued, and the depocenter migrated southward in the Guarga syncline filled by shallow marine and continental upper Eocene–lower Oligocene deposits. Activation of the Guarga thrust during the late Oligocene resulted in a new migration of the depocenter in the Ebro basin [*Teixell*, 1996]. The upper part of the synorogenic sediments deposited along the south Pyrenean thrust yielded ages up to 22 Ma [*Arenas et al.*, 2001], indicating that most of the movement along the Guarga thrust occurred before the middle part of Aquitanian. Minor latest movements are not dated and may have continued during the upper part of Aquitanian and possibly during the Burdigalian [*Millán Garrido et al.*, 2000].

[32] Our data on the Bielsa massif also show that out-of-sequence basement thrusting occurred during the Miocene along the southern edge of the Axial Zone (Figure 8). Depending on the kinematic interpretation adopted for the Bielsa massif exhumation (see discussion in previous section), activity of the Bielsa thrust may have begun during the Burdigalian around 19–18 Ma (central fission track ages on samples BS1 and BS7), but in any case continued more recently in the Miocene (southward tilting of the granite and overlying Gavarnie thrust sheet). We cannot exclude that this late tectonic activity at the southern edge of the Axial Zone was coeval with the youngest, undated movements along the south Pyrenean frontal thrust. However, it seems kinematically difficult that movement of the Bielsa thrust was transmitted to the frontal thrust along the Triassic décollement level that was already severely deformed by the Guarga thrust (Figure 2). It seems more likely that the activity of the Bielsa thrust resulted in internal deformation of the Jaca and Ainsa basins. Such a young deformation has not been recognized in the basin fill up to now and may correspond to out-of-sequence thrusting, back thrusting, distributed deformation or any combination of these.

[33] In the central Pyrenees, apatite fission track analyses by *Fitzgerald et al.* [1999] and *Sinclair et al.* [2005] showed that exhumation of the highest massifs followed a piggy-back sequence of thrusting, i.e., middle-late Eocene for the Riberot massif in the northern part of the Axial Zone, and late Eocene–Oligocene for the Maladetta and the Marimanya massifs in the central part (see location of the massifs in Figure 1). Exhumation of the Maladetta-Marimanya, the highest massif of the central Pyrenees, was thus coeval to that of the Néouvielle massif, the highest massif on the section studied here, but the thrusts involved are not the same. Indeed, the eastward extension of the Gavarnie thrust passes between the Maladetta and Marimanya massifs without being associated with a significant difference in exhumation, which is consistent with a dramatic decrease of offset across the thrust when going eastward [*Soler et al.*, 1998]. The thrust involved in the exhumation of the Maladetta-Marimanya is thus located below and to the south of the Gavarnie thrust. At the south of the Maladetta massif, the small Barruera massif (Figure 1) yielded an exhumation age around 20 Ma, younger than that of the samples located at the same elevation in the Maladetta massif, thus attesting Miocene basement thrusting along the southern edge of the Axial Zone [*Sinclair et al.*, 2005]. Our results on the Bielsa massif thus demonstrate that this late tectonic activity affected a significant length of the Axial Zone.

5. Conclusion

[34] Thermochronology indicates that before the Pyrenean exhumation event, the Néouvielle, Bordère-Louron and Bielsa Variscan granite massifs were buried to depths of at least 4 km (below the fission track annealing zone) and probably less or up to 6–8 km as suggested by the behavior of the biotite and K-feldspar $^{40}Ar/^{39}Ar$ isotopic systems, burial being due to foreland sedimentation and subsequent thrust front propagation.

[35] The $^{40}Ar/^{39}Ar$ ages on K-feldspars from the Néouvielle massif (sample NV7) seem to indicate tectonic movements on the Eaux-Chaudes thrust during the early middle Eocene. The granite massifs were then exhumed by tectonic activity on (1) the Gavarnie thrust at circa 35 Ma for the Néouvielle massif and circa 32 Ma for the Bordère-Louron massif and (2) the Bielsa thrust at circa 19 Ma and younger for the Bielsa massif. Apatite fission track thermochronology provides evidence that the Miocene rapid cooling event that we interpret as resulting from tectonic movements on the Bielsa thrust (exhumation, folding and tilting of the Bielsa granite), is more recent than (1) activity of the Guarga basement thrust located more in the foreland and (2) the earliest Miocene age deduced from deformation of synorogenic sediments for the end of tectonic activity at the southern front of the orogenic prism.

[36] The growth of the Pyrenean accretionary prism thus appears more complex than previously thought. If most of the major basement thrust system generally developed in sequence from north to south (i.e., the Eaux-Chaudes, Gavarnie, and Guarga thrust on the studied section), out-of-sequence faults such as the Bielsa thrust were active after the frontal deformation had stopped. The post-Aquitanian activity in the Axial Zone basement implies shortening and thus out-of-sequence deformation in the Jaca and Ainsa basins that still remains to be described (out-of-sequence cover thrusting, back thrusting, distributed deformation, etc).

[37] Finally, the apatite fission track modeling indicate a last cooling episode starting around 5 Ma which is most certainly related to the Pliocene reexcavation of the southern and northern flanks of the Pyrenees.

[38] **Acknowledgments.** We are very grateful to P. Fitzgerald and one anonymous reviewer for their helpful review of the manuscript. This work was supported by the INSU-CNRS Dyeti program and by the Laboratoire Géosciences Montpellier.

References

Arenas, C., H. Millán, G. Pardo, and A. Pocoví (2001), Ebro basin continental sedimentation associated with late compressional Pyrenean tectonics (northeastern Iberia): Controls on basin margin fans and fluvial systems, *Basin Res.*, *13*, 65–89.

Arnaud, N., P. Tapponnier, F. Roger, M. Brunel, U. Scharer, C. Wen, and X. Zhiqin (2003), Evidence for Mesozoic shear along the western Kunlun and Altyn-Tagh fault, northern Tibet (China), *J. Geophys. Res.*, *108*(B1), 2053, doi:10.1029/2001JB000904.

Babault, J. (2004), Dynamique de l'érosion dans une chaîne de montagnes: Influence de la sédimentation de piedmont: L'exemple des Pyrénées, Ph.D. thesis, 218 pp., Univ. de Rennes 1, Rennes, France.

Babault, J., J. Van Den Driessche, S. Bonnet, S. Castelltort, and A. Crave (2005), Origin of the highly elevated Pyrenean peneplain, *Tectonics*, *24*, TC2010, doi:10.1029/2004TC001697.

Barbarand, J., A. Carter, I. Wood, and T. Hurford (2003), Compositional and structural control of fission-track annealing in apatite, *Chem. Geol.*, *198*, 107–137.

Beaumont, C., J. A. Muñoz, J. Hamilton, and P. Fullsack (2000), Factors controlling the Alpine evolution of the central Pyrenees inferred from a comparison of observations and geodynamical models, *J. Geophys. Res.*, *105*, 8121–8146.

Burtner, R. L., A. Nigrini, and R. A. Donelick (1994), Thermochronology of lower Cretaceous source rocks in the Idaho-Wyoming Thrust Belt, *AAPG Bull.*, *78*, 1613–1636.

Casas, A. M., B. Oliva, T. Román-Berdiel, and E. Pueyo (2003), Basement deformation: Tertiary folding and fracturing of the Variscan Bielsa granite (Axial Zone, central Pyrenees), *Geodyn. Acta*, *16*, 99–117.

Coney, P. J., J. A. Muñoz, K. R. McClay, and C. A. Evenchick (1996), Syntectonic burial and posttectonic exhumation of the southern Pyrenees foreland fold-thrust belt, *J. Geol. Soc. London*, *153*, 9–16.

Dempster, T. J., and C. Persano (2006), Low temperature thermochronology: Resolving geotherm shapes or denudation histories?, *Geology*, *34*, 73–76.

Dodson, M. H. (1973), Closure temperature in cooling geochronological and petrological systems, *Contrib. Mineral. Petrol.*, *40*, 259–274.

Donelick, R. A. (1993), A method of fission track analysis utilizing bulk chemical etching of apatite, U. S. Patent 6,267,274, U. S. Patent Off., Arlington, Va.

Fitzgerald, P. G., J. A. Muñoz, P. J. Coney, and S. L. Baldwin (1999), Asymmetric exhumation across the Pyrenean orogen: Implication for the tectonic evolution of a collisional orogen, *Earth Planet. Sci. Lett.*, *173*, 157–170.

Fitzgerald, P. G., E. M. Duebendorfer, P. B. O'Sullivan, J. E. Faulds, and J. E. Fryxell (2006), The South Virgin-White Hills detachment fault system of SE Nevada and NW Arizona: The application of apatite fission track thermochronology to constraining displacement gradient accommodation along a major detachment fault, *Geochim. Cosmochim. Acta*, *70*(18), Suppl. 1. A177, doi:10.1016/j.gca.2006.06.355.

Garcia-Castellanos, D., J. Vergés, J. Gaspar-Escribano, and S. Cloetingh (2003), Interplay between tectonics, climate, and fluvial transport during the Cenozoic evolution of the Ebro Basin (NE Iberia), *J. Geophys. Res.*, *108*(B7), 2347, doi:10.1029/2002JB002073.

Gleizes, G., D. Leblanc, P. Olivier, and J. L. Bouchez (2001), Strain partitioning in a pluton during emplacement in transpressional regime: The example of the Néouvielle granite (Pyrenees), *Int. J. Earth Sci.*, *90*, 325–340.

Harrison, T. M., and R. L. Armstrong (1978), Thermal models and cooling histories from fission-track, K-Ar, Rb-Sr, and U-Pb mineral dates, northern Coast Pluton Complex, British Colombia (abstract), in *Fourth International Conference on Geochronology, Cosmochronology, and Isotope Geology*, edited by R. E. Zartman, *U. S. Geol. Surv. Open File Rep., 78-701*.

Harrison, T. M., O. M. Lovera, and M. T. Heizler (1991), $^{40}Ar/^{39}Ar$ results for alkali feldspars containing diffusion domains with differing activation energy, *Geochim. Cosmochim. Acta*, *55*, 1435–1448.

Harrison, T. M., M. T. Heizler, O. M. Lovera, C. Wenji, and M. Grove (1994), A chlorine disinfectant for excess argon released from K-feldspar during step heating, *Earth Planet. Sci. Lett.*, *123*, 95–104.

Henderson, I. H. C., and A. M. McCaig (1996), Fluid pressure and salinity variations in shear zone related veins, central Pyrenees, France: Implications for the fault-valve model, *Tectonophysics*, *262*, 321–348.

Hurford, A. J. (1990), Standardization of fission track dating calibration: Recommendation by the Fission track Working Group of the IUGS Subcommission on Geochronology, *Chem. Geol.*, *80*, 171–178.

Hurford, A. J., and P. F. Green (1983), The zeta age calibration of fission-track dating, *Chem. Geol.*, *1*, 285–317.

Ingles, J., C. Lamouroux, J. C. Soula, N. Guerrero, and P. Debat (1999), Nucleation of ductile shear zones in a granodiorite under greenschist facies conditions, Néouvielle massif, Pyrenees, France, *J. Struct. Geol.*, *21*, 555–576.

Ketcham, R. A., R. A. Donelick, and W. D. Carlson (1999), Variability of apatite fission-track annealing kinetics: III. Extrapolation to geological time scales, *Am. Mineral.*, *84*, 1235–1255.

Ketcham, R. A., R. A. Donelick, and M. B. Donelick (2000), AFTSolve: A program for multikinetic modelling of apatite fission-track data, *Geol. Mater. Res.*, *2*, 1–32.

Labaume, P., M. Séguret, and C. Seyve (1985), Evolution of a turbiditic foreland basin and analogy with an accretionary prism: Example of the Eocene south-Pyrenean basin, *Tectonics*, *4*, 661–685.

Lamouroux, C., P. Debat, J. Déramond, and C. Majesté-Menjoulas (1979), Influence des massifs plutoniques hercyniens dans l'évolution des structures pyrénéennes: Exemple du massif du Néouvielle, *Bull. Soc. Geol. Fr.*, *7*, 213–220.

Laslett, G. M., P. F. Green, I. R. Duddy, and A. J. W. Gleadow (1987), Thermal annealing of fission tracks in apatite, 2. A quantitative analysis, *Chem. Geol.*, *65*, 1–13.

Lovera, O. M. (1992), Computer program to model $^{40}Ar/^{39}Ar$ diffusion data from multidomain samples, *Comput. Geosci.*, *18*, 789–813.

Lovera, O. M., F. M. Richter, and T. M. Harrison (1989), The $^{40}Ar/^{39}Ar$ thermochronometry for slowly cooled samples having a distribution of diffusion domain sizes, *J. Geophys. Res.*, *94*, 17,917–17,935.

Lovera, O. M., F. M. Richter, and T. M. Harrison (1991), Diffusion domains determined by ^{39}Ar released during step heating, *J. Geophys. Res.*, *96*, 2057–2069.

Maurel, O. (2003), L'exhumation de la zone axiale des Pyrénées orientales: Une approche thermo-chronologique multi-méthodes du rôle des failles, thèse de Doctorat, 219 pp., Univ. Montpellier II, Montpellier, France.

Maurel, O., J. P. Respaut, P. Monie, N. O. Arnaud, and M. Brunel (2004), Emplacement and $^{40}Ar/^{39}Ar$ cooling ages of the eastern Mont-Louis granite massif (eastern Pyrenees, France), *C. R. Geosci.*, *336*, 1091–1098.

Millán Garrido, H., E. L. Pueyo Morer, M. Aurell Cardona, A. Aguado Luzón, B. Oliva Murcia, M. B. MartínezPeña, and A. Pocoví Juan (2000), Actividad tectonica registrada en los depositos terciarios del frente meridional del Pirineo central, *Rev. Soc. Geol. Esp.*, *13*, 279–3000.

Millán Garrido, H., B. Oliva Murcia, and A. Pocoví Juan (2006), La transversal de Gavarnie-Guara. Estructura y edad de los mantos de Gavarnie, Guara-Gèdre y Guarga (Pirineo centro occidental), *Geogaceta*, *40*, 35–38.

Monié, P., R. Caby, and M. H. Arthaud (1997), The Neoproterozoic Brasiliano Orogeny in northeast Brazil; $^{40}Ar/^{39}Ar$ and petrostructural data from Ceara, *Precambrian Res.*, *81*, 241–264.

Morris, R. G., H. D. Sinclair, and A. J. Yelland (1998), Exhumation of the Pyrenean orogen: Implications for sediment discharge, *Basin Res.*, *10*, 69–85.

Muñoz, J. A. (1992), Evolution of a continental collision belt: ECORS-Pyrenes crustal balanced cross-section, in *Thrust Tectonics*, edited by K. R. McClay, pp. 235–246, Chapman and Hall, New York.

Mutti, E., M. Séguret, and M. Sgavetti (1988), Sedimentation and deformation in the Tertiary sequences of the southern Pyrenees, in *AAPG Mediterranean Basins Conference, Field Trip 7*, special publication, 157 pp., Inst. of Geol., Univ. of Parma, Parma, Italy.

Nelson, C. H., and A. Maldonado (1990), Factors controlling late Cenozoic continental margin growth from the Ebro Delta to the western Mediterranean deep sea, *Mar. Geol.*, *95*, 419–440.

Román-Berdiel, T., A. M. Casas, B. Oliva-Urcia, L. Pueyo, and C. Rillo (2004), The main Variscan deformation event in the Pyrenees: New data from the structural study of the Bielsa granite, *J. Struct. Geol.*, *26*, 659–677.

Roure, F., P. Choukroune, X. Berastegui, J. A. Muñoz, A. Villien, P. Matheron, M. Bareyt, M. Séguret, P. Camara, and J. Déramond (1989), ECORS deep seismic data and balanced cross sections: Geometric constraints on the evolution of the Pyrenees, *Tectonics*, *8*, 41–50.

Séguret, M. (1972), Etude tectonique des nappes et séries décollées de la partie centrale du versant sud des Pyrénées. Caractère synsédimentaire, rôle de la compression et de la gravité, *Ser. Geol. Struct.*, *2*, 155 pp., Univ. des Sci. et Tech. du Languedoc, Montpellier, France.

Sinclair, H. D., M. Gibson, M. Naylor, and R. G. Morris (2005), Asymmetric growth of the Pyrenees revealed through measurement and modelling of orogenic fluxes, *Am. J. Sci.*, *305*, 369–406.

Soler, D., A. Teixell, and J. Garcia-Sansegundo (1998), Amortissement latéral du chevauchement de Gavarnie et sa relation avec les unités sud-pyrénéennes, *C. R. Acad. Sci.*, *327*, 699–704.

Teixell, A. (1996), The Ansó transect of the southern Pyrenees: Basement and cover thrust geometries, *J. Geol. Soc.*, *153*, 301–310.

Teixell, A. (1998), Crustal structure and orogenic material budget in west central Pyrenees, *Tectonics*, *17*, 395–406.

Teixell, A., and J. A. Muñoz (2000), Evolución tectono-sedimentaria del Pirineo meridional durante el Terciario: Una sintesis basada en la transversal del rio Noguera Ribagorçana, *Rev. Soc. Geol. Esp.*, *13*, 251–264.

Vergés, J., M. Fernández, and A. Martínez (2002), The Pyrenean orogen: Pre-, syn-, and postcollisional evolution, *J. Virtual Explor.*, *8*, 57–76.

Wayne, D. M., and A. M. McCaig (1998), Dating fluid flow in shear zones: Rb-Sr and U-Pb studies of syntectonic veins in the Néouvielle massif, Pyrenees, in *Dating and Duration of Fluid Flow and Fluid-Rock Interaction*, edited by J. Parnell, *Geol. Soc. Spec. Publ.*, *144*, 129–135.

N. Arnaud, M. Brunel, M. Jolivet, P. Labaume, and P. Monié, Laboratoire Géosciences Montpellier (cc060), CNRS-UMR 5243, Université Montpellier II, F-34095 Montpellier cedex 5, France. (jolivet@gm.univ-montp2.fr)

M. Campani, Geology Institute, ETH Zentrum, Leonhardstrasse 19/LEB, CH-8092 Zurich, Switzerland.